

1-1-2006

## Synthesis and Characterization of LiFePO<sub>4</sub> and LiTi<sub>0.01</sub>Fe<sub>0.99</sub>PO<sub>4</sub> Cathode Materials

G. X. Wang

*University of Wollongong, gwang@uow.edu.au*

S. Bewlay

*University of Wollongong*

Scott A. Needham

*University of Wollongong, scottn@uow.edu.au*

Hua-Kun Liu

*University of Wollongong, hua@uow.edu.au*

R. C. Liu

*National Taiwan University, Taiwan*

*See next page for additional authors*

Follow this and additional works at: <https://ro.uow.edu.au/engpapers>



Part of the [Engineering Commons](#)

<https://ro.uow.edu.au/engpapers/111>

---

### Recommended Citation

Wang, G. X.; Bewlay, S.; Needham, Scott A.; Liu, Hua-Kun; Liu, R. C.; Drozd, V. A.; Lee, J. F.; and Chen, J. M.:  
Synthesis and Characterization of LiFePO<sub>4</sub> and LiTi<sub>0.01</sub>Fe<sub>0.99</sub>PO<sub>4</sub> Cathode Materials 2006.  
<https://ro.uow.edu.au/engpapers/111>

---

**Authors**

G. X. Wang, S. Bewlay, Scott A. Needham, Hua-Kun Liu, R. C. Liu, V. A. Drozd, J. F. Lee, and J. M. Chen



## Synthesis and Characterization of $\text{LiFePO}_4$ and $\text{LiTi}_{0.01}\text{Fe}_{0.99}\text{PO}_4$ Cathode Materials

G. X. Wang,<sup>a,b,z</sup> S. Bewlay,<sup>a</sup> S. A. Needham,<sup>a</sup> H. K. Liu,<sup>a,b,\*</sup> R. S. Liu,<sup>c</sup>  
V. A. Drozd,<sup>c</sup> J.-F. Lee,<sup>d</sup> and J. M. Chen<sup>d</sup>

<sup>a</sup>Institute for Superconducting and Electronic Materials and <sup>b</sup>ARC Centre of Excellence for Nanostructured Electromaterials, University of Wollongong, Wollongong, New South Wales 2500, Australia

<sup>c</sup>Department of Chemistry, National Taiwan University, Taipei 106, Taiwan

<sup>d</sup>National Synchrotron Radiation Research Centre, Hsinchu 300, Taiwan

Nanocrystalline  $\text{LiFePO}_4$  and doped  $\text{LiTi}_{0.01}\text{Fe}_{0.99}\text{PO}_4$  powders were synthesized via a sol-gel preparation route. High-resolution tunneling electron microscopy observation and energy dispersive spectroscopy, mapping show the homogeneous distribution of dopant Ti cations in the crystals. Fe and O *K*-edge X-ray absorption near-edge structure (XANES) measurements show that  $\text{Ti}^{4+}$  doping induces an increased unoccupied d-state in  $\text{LiFePO}_4$ , resulting in an enhanced p-type semiconductivity. In situ Fe *K*-edge XANES measurements of Ti-doped and undoped  $\text{LiFePO}_4$  electrodes have been performed to determine the change of Fe valence during the lithium intercalation and de-intercalation processes. Both  $\text{LiFePO}_4$  and doped  $\text{LiTi}_{0.01}\text{Fe}_{0.99}\text{PO}_4$  cathodes demonstrate good electrochemical performance.

© 2005 The Electrochemical Society. [DOI: 10.1149/1.2128766] All rights reserved.

Manuscript submitted June 2, 2005; revised manuscript received August 25, 2005. Available electronically November 22, 2005.

The growing demand for portable electronic devices has driven successful development of advanced lithium-ion batteries with high energy density. The current lithium-ion batteries are based on the chemistry of the  $\text{LiCoO}_2$  cathode and carbon anode.<sup>1</sup> Due to the toxicity, high cost, and safety concerns,  $\text{LiCoO}_2$  cathode materials are limited to small lithium-ion battery applications. There has been intensive research on developing new cathode materials such as  $\text{LiMn}_2\text{O}_4$  spinels,<sup>2-5</sup> lithium nickel based oxides,<sup>6-8</sup> and layered  $\text{LiMnO}_2$ <sup>9-11</sup> compounds, etc.

Iron-based cathode materials are ideal for future lithium-ion batteries in terms of low cost and environmental friendliness. In particular, they are very suitable as cathode materials for large-size lithium-ion batteries in applications related to electric vehicles (EVs), hybrid electric vehicles (HEVs), and stationary storage batteries. Layered  $\text{LiFeO}_2$  has been synthesized for reversible lithium extraction/insertion. However,  $\text{Li}_x\text{FeO}_2$  is not stable and shows a low average voltage vs  $\text{Li/Li}^+$ .<sup>12,13</sup> A group of lithium- and iron-containing compounds incorporating polyanions of the class  $\text{XO}_4^{3-}$  ( $\text{X} = \text{S}, \text{P}, \text{As}, \text{Mo}$ ) has been explored recently.<sup>14-16</sup> The large polyanions can stabilize the structure and tune the  $\text{Fe}^{3+}/\text{Fe}^{2+}$  redox potential to a useful level. Among them,  $\text{LiFePO}_4$  with a theoretical capacity of 170 mAh/g has emerged as a new cathode material for lithium-ion batteries. The extraction of lithium from  $\text{LiFePO}_4$  to form  $\text{FePO}_4$  induces a 6.81% volume decrease in the cathode. This shrinkage compensates for the volume expansion of the carbon anode during the charging process.  $\text{LiFePO}_4$  has an olivine structure (space group: *Pnma*), in which Li, Fe, and P atoms, respectively, occupy octahedral 4a, octahedral 4c, and tetrahedral 4c sites. The oxygen atoms are in a slightly distorted, hexagonal close-packed arrangement. The  $\text{FeO}_6$  octahedra share common corners in the *bc* plane, and  $\text{LiO}_6$  octahedra form an edge-sharing chain in the *b* direction. The separation of the  $\text{FeO}_6$  octahedra by  $\text{PO}_4$  polyanions significantly reduces the electrical conductivity of materials, leading to poor rate capacity and low utilization of Li in the  $\text{LiFePO}_4$  host structure. Many efforts have been made to overcome this problem, including carbon coating,<sup>17,18</sup> addition of conductive copper/silver powders,<sup>19</sup> dispersing carbon black with high surface area,<sup>20</sup> supervalence cation doping,<sup>21</sup> and synthesis of small grains.<sup>22</sup> In this paper, we report the synthesis of  $\text{LiFePO}_4$  and doped  $\text{LiTi}_{0.01}\text{Fe}_{0.99}\text{PO}_4$  cathode materials by using the sol-gel method. The conductivity of

$\text{LiFePO}_4$  was found to be enhanced via  $\text{Ti}^{4+}$  doping. The physical, structural, and electrochemical properties of  $\text{LiFePO}_4$  compounds were systematically investigated.

### Experimental

$\text{LiFePO}_4$  and doped  $\text{LiTi}_{0.01}\text{Fe}_{0.99}\text{PO}_4$  were synthesized via a sol-gel preparation route.  $\text{LiOH}\cdot\text{H}_2\text{O}$  (99.9%, Aldrich),  $\text{FeC}_2\text{O}_4\cdot 2\text{H}_2\text{O}$  (99%, Aldrich),  $\text{NH}_4\text{H}_2\text{PO}_4$  (97%, Aldrich), and  $\text{Ti}(\text{OCH}_3)_4$  (99%, Aldrich) were used as reactants. The stoichiometric amounts of reactants were dissolved in deionized water, in which polyacrylic acid and citric acid were added as complexing agents for the formation of the gel. The solutions were heated and maintained at 85°C under vigorous stirring until a viscous gel was formed. The as-formed gel was heated to 500°C to decompose the organic components under flowing argon gas. The decomposed precursors were further sintered at 750°C under a flowing gas mixture (10%  $\text{H}_2$  in Ar). A reducing atmosphere was employed during the sintering process in order to prevent the oxidation of  $\text{Fe}^{2+}$  cations.

X-ray diffraction was performed on the prepared lithium iron phosphates to determine the phase purity using Cu  $\text{K}\alpha$  radiation ( $\text{MO3xHF22}$ , MacScience, Japan). The morphology of lithium iron phosphate powders was studied using a high-resolution transmission electron microscope (HRTEM, 300 kV JEOL JEM-3000F with field emission).

Electrochemical characterization was performed by assembling CR2032 coin cells for galvanostatic charge/discharge. The electrodes were made by dispersing 80 wt % active material, 10 wt % carbon black, and 10 wt % polyvinylidene fluoride (PVDF) in *n*-methyl pyrrolidone (NMP) to form a slurry. The slurry was then coated onto an Al foil. The coated electrodes were dried in a vacuum oven and then pressed at 1200 kg/cm<sup>2</sup>. The coin cells were assembled in a argon-filled glove box (Mbraun, Unilab, Germany) with a lithium foil as the counter electrode. The electrolyte was 1 M  $\text{LiPF}_6$  in a 1:1 mixture of ethylene carbonate (EC) and dimethyl carbonate (DMC). For in situ X-ray absorption studies, Mylar windows were used to allow the penetration of the synchrotron beam. Cyclic voltammetry (CV) measurements were performed using a CHI660B electrochemical working station at a scanning rate of 0.1 mV/s. The cells were galvanostatically charged and discharged at C/8 rate over a voltage range of 2.75–4.3 V.

The synchrotron-based X-ray absorption experiments were carried out at the National Synchrotron Radiation Research Center in Taiwan. The electron storage ring was operated at an energy of 1.5 GeV with a beam current of 100–200 mA. The Fe *K*-edge XANES spectra were performed at the BL17C Wiggler beamline. A Si(111) double-crystal monochromator was used for energy selec-

\* Electrochemical Society Active Member.

<sup>z</sup> E-mail: gwang@uow.edu.au.

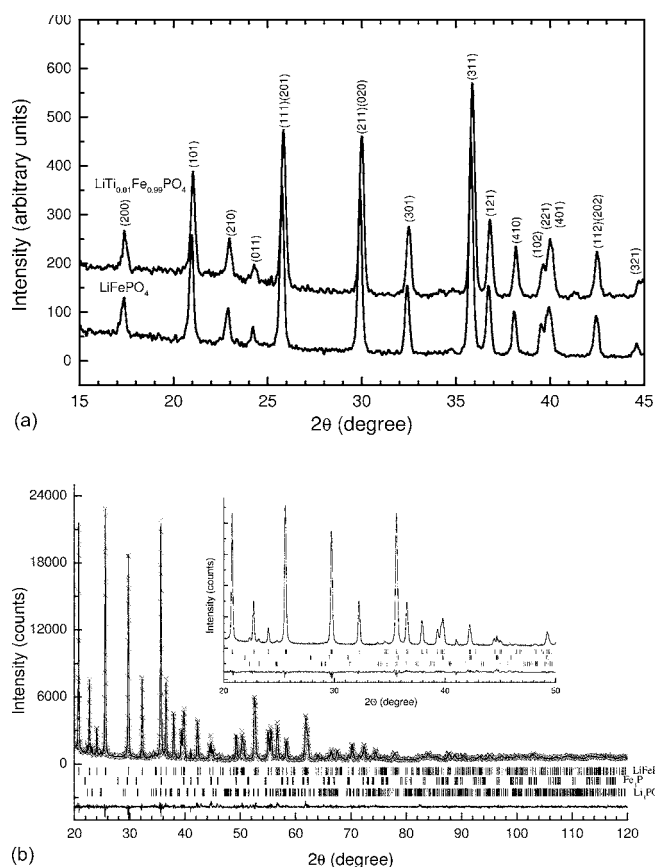


**Figure 1.** (a) X-ray diffraction patterns of  $\text{LiFePO}_4$  and  $\text{LiTi}_{0.01}\text{Fe}_{0.99}\text{PO}_4$  powders. (b) Rietveld refinement of  $\text{LiTi}_{0.01}\text{Fe}_{0.99}\text{PO}_4$  sample.

tion with a resolution ( $\Delta E/E$ ) of about  $2 \times 10^{-4}$ . The XANES spectra at the Fe  $K$ -edge were recorded at room temperature in transmission mode using gas-filled ionization chambers to measure the intensities of the incident ( $I_0$ ), transmitted ( $I_t$ ), and reference ( $I_{\text{ref}}$ ) signals. A 7  $\mu\text{m}$  thick iron foil was used as a reference. Both Fe foil and  $I_{\text{ref}}$  detector were positioned downstream the sample (in situ cell) along the X-ray beam direction. The data from three scans were averaged, and the background was subtracted. The XANES spectra were normalized with respect to the edge jump step.

The O 1s XANES measurements were performed on the BL20A high-energy spherical grating monochromator (HSGM) beamline. The O  $K$ -edge XANES spectra were recorded in X-ray fluorescence-yield and electron-yield mode. The X-ray fluorescence yield was measured by utilizing a microchannel-plate (MCP) detector system.

Photons were incident at an angle of  $45^\circ$  with respect to the sample normal. In the electron-yield mode, the sample drain current is measured. Simultaneously to X-ray fluorescence yield and electron yield, the incident photon flux was monitored by a Ni mesh located after the exit slit of the monochromator. The photon energies were calibrated with an accuracy of 0.1 eV using the known O  $K$ -edge absorption peaks of a  $\text{CuO}$  compound. The X-ray fluorescence-yield absorption spectra were normalized to  $I_0$  and subsequently corrected for self-absorption effects. The energy resolution of the monochromator was set to  $\sim 0.22$  eV at the O 1s absorption edge.

## Results and Discussion

**Physical characteristics of  $\text{LiFePO}_4$  and  $\text{LiTi}_{0.01}\text{Fe}_{0.99}\text{PO}_4$ .**—X-ray diffraction patterns of  $\text{LiFePO}_4$  and  $\text{LiTi}_{0.01}\text{Fe}_{0.99}\text{PO}_4$  samples are shown in Fig. 1a. All diffraction lines of  $\text{LiFePO}_4$  are indexed to an orthorhombic crystal structure (triphylite, space group  $Pnma$ ). Ti-doped sample contains  $\text{Li}_3\text{PO}_4$  and  $\text{Fe}_3\text{P}$  as impurity phases. These phases are usually reported as impurities in aliovalent-doped  $\text{LiFePO}_4$  samples.<sup>22</sup>

We performed Rietveld refinement on the X-ray diffraction patterns using GSAS (General Structure Analysis System) to obtain the crystal structure parameters.<sup>23</sup> Impurity phases,  $\text{Li}_3\text{PO}_4$  and  $\text{Fe}_3\text{P}$ , were included in Rietveld refinement for Ti-doped sample. For  $\text{Fe}_3\text{P}$  phase, strong preferred orientation of  $\{211\}$  reflection was observed and it was also taken into account during the refinement (as shown in Fig. 1b). Crystal structure characteristics of  $\text{LiFePO}_4$  and  $\text{LiFe}_{0.99}\text{Ti}_{0.01}\text{PO}_4$  are summarized in Table I and Table II, respectively. The refinement of Fe site occupancy of Ti-doped sample leads to the value 0.984, which is close to the stoichiometric index of iron in chemical formula of Ti-doped sample, demonstrating proper substitution of dopant ions. We also tried to include Ti in refinement but the obtained value is much higher than actual Ti content in the sample.

$\text{LiFePO}_4$  has lattice parameters  $a = 10.3148(1)$  Å,  $b = 6.0009(7)$  Å,  $c = 4.6897(5)$  Å,  $V = 290.28(5)$  Å<sup>3</sup>, while the doped  $\text{LiTi}_{0.01}\text{Fe}_{0.99}\text{PO}_4$  has slightly varied lattice parameters:  $a = 10.3233(2)$  Å,  $b = 6.00313(8)$  Å,  $c = 4.69694(7)$  Å,  $V = 291.077(7)$  Å<sup>3</sup>. The unit cell of the crystal lattice was slightly expanded along all  $x$ -,  $y$ -, and  $z$  directions due to the Ti doping effect.  $\text{Fe}^{2+}$  ions are located at the center of a distorted  $\text{FeO}_6$  octahedron in the  $\text{LiFePO}_4$  olivine structure. The Fe–O distances calculated from the Rietveld refinement range from 2.058 to 2.246 Å. Each octahedron is connected to four other  $\text{FeO}_6$  octahedra and four  $\text{PO}_4$  tetrahedra, and shares edges with  $\text{PO}_4$  tetrahedra. The P ions share a common oxygen nearest neighbor with Fe along a Fe–O–P linkage. Therefore, the strength of the covalent Fe–O bond is weakened via the inductive effect of the Fe–O–P linkage and electrostatic repulsion between Fe and P. This induces a high open-circuit voltage (OCV) of the  $\text{Fe}^{2+}/\text{Fe}^{3+}$  redox pair with respect to the Fermi level of

**Table I.** Structure parameters of  $\text{LiFePO}_4$  determined from X-ray diffraction at 300 K.

Atoms	$x$	$y$	$z$	Occupancy	$U_{\text{iso}}$ (Å <sup>2</sup> )	Interatomic distances (Å)	
Li	0	0	0	1	0.014(6)	Fe–O(1) $\times$ 1	2.235(1)
Fe	0.2823(2)	0.25	0.9740(5)	1	0.011(7)	Fe–O(2) $\times$ 1	2.108(1)
						Fe–O(3) $\times$ 2	2.235(6)
						Fe–O(3) $\times$ 2	2.058(6)
						Fe–O average	2.155
P	0.0955(3)	0.25	0.4221(8)	1	0.014(3)	P–O(1) $\times$ 1	1.512(7)
O(1)	0.0924(1)	0.25	0.7445(2)	1	0.014(3)	P–O(2) $\times$ 1	1.597(1)
O(2)	0.4542(2)	0.25	0.2170(2)	1	0.010(3)	P–O(3) $\times$ 2	1.569(7)
O(3)	0.1677(9)	0.0467(1)	0.2836(1)	1	0.012(2)	P–O average	1.562
Space group: $Pnma$ (orthorhombic)						Bond angles (degrees)	
Unit cell parameters: $a = 10.3148(1)$ Å, $b = 6.0009(7)$ Å, $c = 4.6897(5)$ Å, cell volume: $290.28(5)$ Å <sup>3</sup>						O(3)–Fe(2)–O(3)	91.3(4)
Reliability factors						O(3)–Fe(2)–O(3)	119.8(4)
$R_p = 4.88\%$ , $R_{wp} = 6.55\%$							
$\chi^2 = 0.63$							

**Table II.** Structure parameters of  $\text{LiTi}_{0.01}\text{Fe}_{0.99}\text{PO}_4$  determined from X-ray diffraction at 300 K.

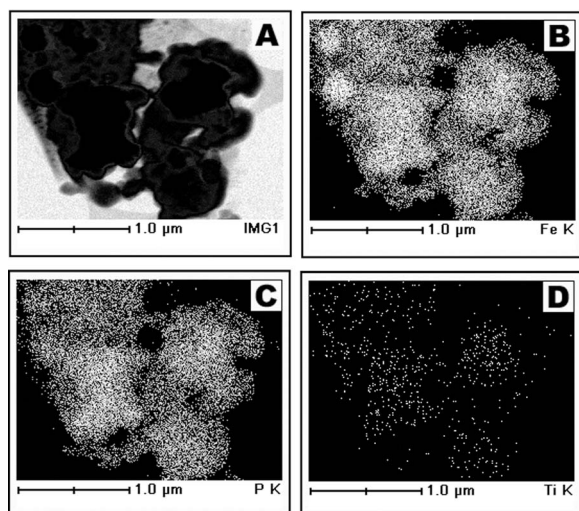
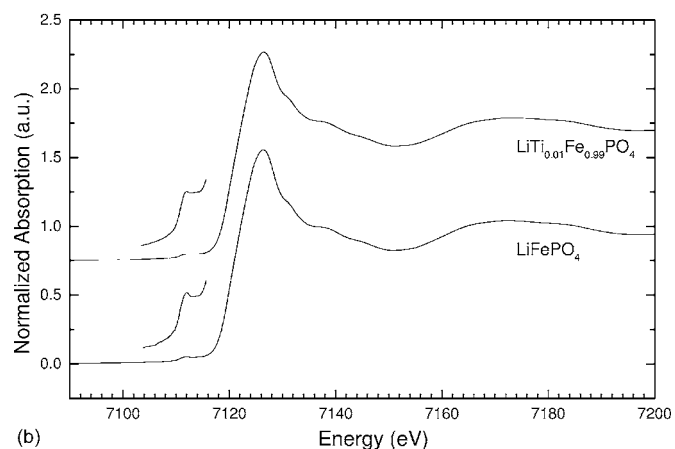
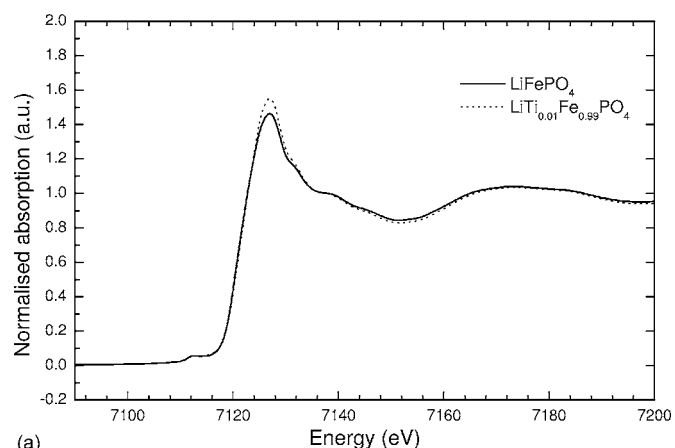
Atoms	<i>x</i>	<i>y</i>	<i>z</i>	Occupancy	$U_{\text{iso}} \cdot 100(\text{\AA}^2)$	Interatomic distances ( $\text{\AA}$ )	
Li	0	0	0	1	1.3(3)	Fe–O(1) $\times$ 1	2.17158(2)
Fe	28,198(9)	0.25	0.9763(3)	0.984(1)	1.18(3)	Fe–O(2) $\times$ 1	2.06936(2)
						Fe–O(3) $\times$ 2	2.22091(2)
						Fe–O(3) $\times$ 2	2.05327(2)
						Fe–O average	2.1316
P	0.0955(2)	0.25	0.4179(4)	1	1.05(5)	P–O(1) $\times$ 1	1.53393(2)
O(1)	0.1000(4)	0.25	0.7443(7)	1	0.4(1)	P–O(2) $\times$ 1	1.57062(2)
O(2)	0.4537(5)	0.25	0.2035(7)	1	1.9(1)	P–O(3) $\times$ 2	1.58032(1)
O(3)	0.1696(5)	0.0452(5)	0.2829(5)	1	0.80(9)	P–O average	1.5663
Space group: <i>Pnma</i> (orthorhombic)					Reliability factors		Bond angles (degrees)
Unit cell parameters: $a = 10.3233(2) \text{ \AA}$ , $b = 6.00313(8) \text{ \AA}$ , $c = 4.69694(7) \text{ \AA}$ , cell volume: $291.077(7) \text{ \AA}^3$					$R_{\text{wp}} = 5.02\%$ , $R_p = 6.97\%$		O(3)–Fe(2)–O(3)
					$\chi^2 = 0.471$		O(3)–Fe(2)–O(3)
							91.108(1)
							119.347(1)

lithium. The small amount of Ti doping would not disturb or change the OCV of lithium iron phosphate cathode materials because it is mainly determined by polyanion  $\text{PO}_4^{3-}$ .

During the synthesis of  $\text{LiFePO}_4$  and  $\text{LiTi}_{0.01}\text{Fe}_{0.99}\text{PO}_4$  compounds, the ingredient  $\text{Li}^+$ ,  $\text{Fe}^{2+}$ ,  $\text{Ti}^{4+}$ , and  $\text{PO}_4^{3-}$  ions were dissolved in the water-based solution and mixed on the atomic scale. Therefore, the Ti dopant ions should be distributed homogeneously in the  $\text{LiFePO}_4$  crystal structure despite the presence of some amounts of the impurities. A uniform distribution of the Fe and P elements is also expected. We performed elemental mapping on  $\text{LiTi}_{0.01}\text{Fe}_{0.99}\text{PO}_4$  grains by HRTEM. Figure 2 shows the elemental mapping of Fe, P, and Ti in  $\text{LiTi}_{0.01}\text{Fe}_{0.99}\text{PO}_4$  compound. A very homogeneous elemental distribution was observed in  $\text{LiTi}_{0.01}\text{Fe}_{0.99}\text{PO}_4$  grains. In particular, energy dispersive spectroscopy (EDS) mapping shows the uniform distribution of the trace dopant element  $\text{Ti}^{4+}$  ions on the surface of the individual crystals. This observation confirms the advantages of the sol-gel synthesis process.

*Ex situ XANES measurements on  $\text{LiFePO}_4$  and  $\text{LiTi}_{0.01}\text{Fe}_{0.99}\text{PO}_4$  powders.*—Figure 3a shows a comparison of the Fe *K*-edge XANES spectra of undoped  $\text{LiFePO}_4$  and Ti-doped  $\text{LiTi}_{0.01}\text{Fe}_{0.99}\text{PO}_4$ . The Fe *K*-edge XANES spectra consist of two main parts, the pre-edge and the main edge regions. The pre-edge peak is located to the lower energy side of the sharply rising absorption edge (white line), corresponding to the  $1s \rightarrow 3d$  electronic transition. As shown in Fig. 3, the doped  $\text{LiTi}_{0.01}\text{Fe}_{0.99}\text{PO}_4$  exhibits an increased white line ( $\sim 7125 \text{ eV}$ ) intensity over that of undoped

$\text{LiFePO}_4$ . The increase in the white line intensity reflects the increased number of unoccupied d-states for Fe ions in the surface layer of  $\text{LiFePO}_4$  particles.<sup>24,25</sup> The 3d and 4s orbitals are all empty in  $\text{Ti}^{4+}$  ions. There are 4 valence electrons in 3d orbit in  $\text{Fe}^{2+}$  ions. Therefore, when  $\text{Ti}^{4+}$  is substituted for  $\text{Fe}^{2+}$ ,  $\text{Ti}^{4+}$  ions would be able to attract 3d electrons from  $\text{Fe}^{2+}$ , creating positive holes in the 3d states in  $\text{Fe}^{2+}$  ions. This effect induces an increased p-type conductivity. Previously, Chiang et al. found that supervalent doping of

**Figure 2.** Elemental mapping by scanning TEM (STEM).**Figure 3.** (a) The comparison of the white line intensities of Fe *K*-edge XANES spectra for  $\text{LiFePO}_4$  and doped  $\text{LiTi}_{0.01}\text{Fe}_{0.99}\text{PO}_4$  powders. (b) Separate Fe *K*-edge XANES spectra of  $\text{LiFePO}_4$  and doped  $\text{LiTi}_{0.01}\text{Fe}_{0.99}\text{PO}_4$  powders (the intensities of the pre-edge region are magnified 10 times for clarity).



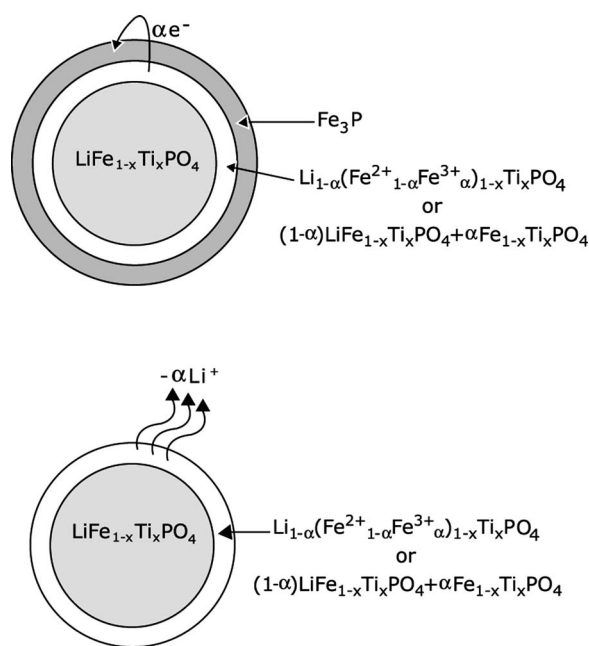
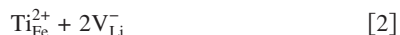


**Figure 4.** Two models describing increase in hole concentration on the surface of  $\text{LiTi}_{0.01}\text{Fe}_{0.99}\text{PO}_4$  particles.

$\text{LiFePO}_4$  compounds results in extrinsic p-type semiconductors.<sup>21</sup> Our Fe K-edge XANES measurement has identified a similar finding.

Despite the multiphase nature of Ti-doped sample, according to scanning transmission electron microscopy (STEM) the Ti distribution within  $\text{LiFePO}_4$  particles is homogeneous, which may be evidence of Ti substitution for Fe in the olivine structure. In this case charge compensation can be achieved via vacancies formation in either Fe or Li sublattices. Using Kroger-Vink defect notation, this can be illustrated as follows



These two mechanisms are illustrated as two models in Fig. 4. The first scheme describes  $\text{LiFe}_{1-2x}\text{Ti}_x\text{PO}_4$  chemical formula and the second corresponds to  $\text{Li}_{1-2x}\text{Fe}_{1-x}\text{Ti}_x\text{PO}_4$ . However, none of these two mechanisms itself can give rise to enhanced charge carrier concentration or explain increase in hole concentration on the surface of  $\text{LiFePO}_4$  particles. However, we suggest that the second mechanism of charge compensation might increase Li-ion mobility in the olivine structure and improve electrochemical performance of the material only with a small degradation of overall capacity due to the decrease of Li-ion content per formula unit.

Strong preferred orientation of  $\text{Fe}_3\text{P}$  phase which is present in the sample in a relatively small amount can be explained if it forms thin epitaxial layer on the surface of  $\text{LiFePO}_4$  particles. In this case, the X-ray absorption spectroscopy (XAS) behavior of the surface and bulk of  $\text{LiFePO}_4$  particles will be different. Presence on the surface of  $\text{LiFePO}_4$  of the thin layer of reduced iron phosphide,  $\text{Fe}_3\text{P}$ , will cause charge transfer from the bulk of material and an increase in intensity of white line in the XAS spectrum of Ti-doped lithium iron phosphate.

In order to identify the features of the pre-edge, the pre-edge region of the spectra was magnified 10 times in Fig. 3b. The pre-edge peak is the most salient and useful characteristic for determining the Fe oxidation state and coordination environment. The pre-edge peak of Fe 1s edge represents  $1s \rightarrow 3d$  quadrupolar electronic transition, which is a dipole forbidden process. However, it becomes partially allowed due to the mixing of d-states of Fe with the p-states

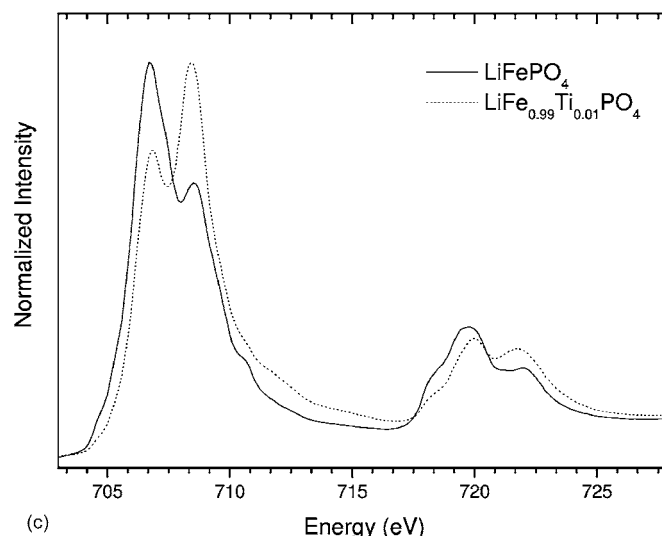
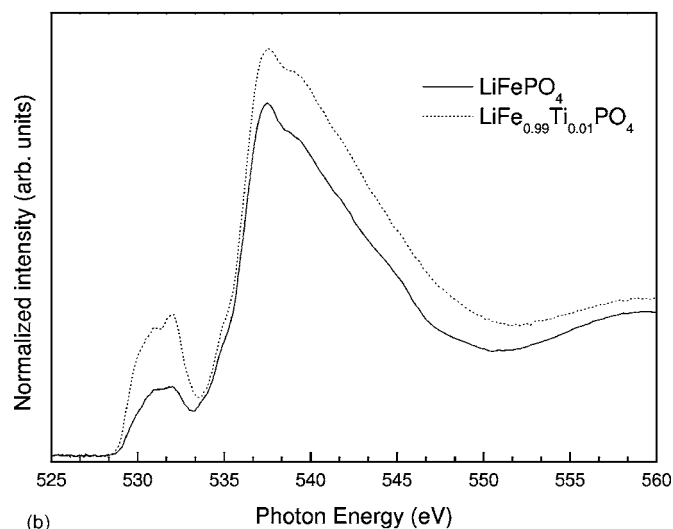
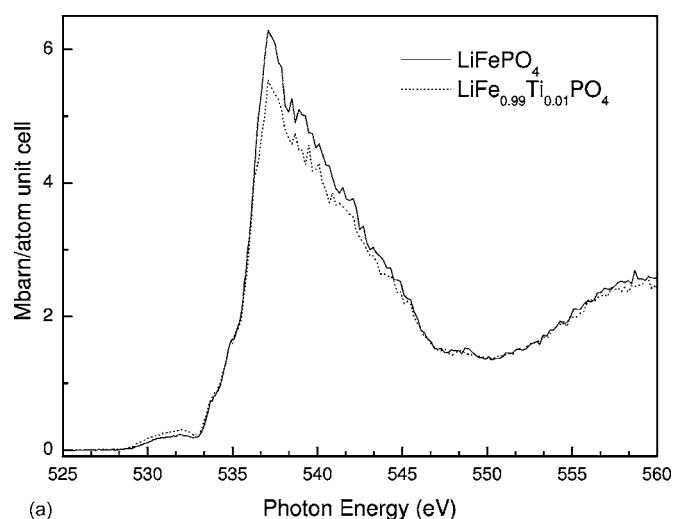


**Figure 5.** (a) Oxygen K-edge X-ray absorption spectra of pristine  $\text{LiFePO}_4$  and  $\text{LiFe}_{0.99}\text{Ti}_{0.01}\text{PO}_4$  measured in FY mode. (b) EY modes. (c) Fe L-edge X-ray absorption spectra of pristine  $\text{LiFePO}_4$  and  $\text{LiFe}_{0.99}\text{Ti}_{0.01}\text{PO}_4$  measured in electron yield mode. Spectra are normalized at high energy region.

of the surrounding oxygen atoms and deviation of Fe ion coordination geometry from ideal octahedron. The energy positions of the

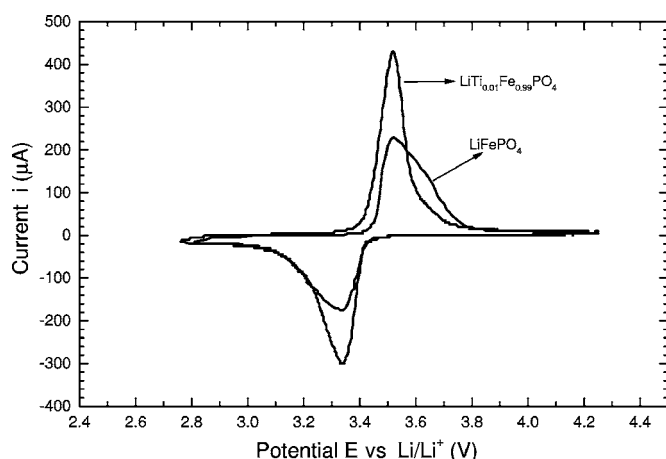


**Figure 6.** Cyclic voltammograms of  $\text{LiFePO}_4$  and doped  $\text{LiTi}_{0.01}\text{Fe}_{0.99}\text{PO}_4$  electrodes.

pre-edge peak are sensitive to the Fe oxidation state, while the intensity of the pre-edge peak depends on site centrosymmetry, with the most centrosymmetric Fe coordinations having the lowest intensity. Therefore, it will be at the lowest intensity for octahedral symmetry ( $O_h$ ) and reach the maximum in the case of tetrahedral coordination ( $T_d$ ). The pre-edge peak position observed is 7111.9 eV for both  $\text{LiFePO}_4$  and  $\text{LiTi}_{0.01}\text{Fe}_{0.99}\text{PO}_4$ . It is the same energy observed for  $\text{Fe}^{2+}$  previously,<sup>26</sup> which proves that the valence of Fe in the bulk of  $\text{LiFePO}_4$  and  $\text{LiTi}_{0.01}\text{Fe}_{0.99}\text{PO}_4$  is +2. There is no variation of pre-edge peak position and intensity due to Ti doping, which confirms that the trace amount of dopant  $\text{Ti}^{4+}$  ions does not disturb the oxidation state of Fe or the structural coordination in  $\text{LiFePO}_4$  crystals. The pre-edge peak energy for  $\text{Fe}^{3+}$  in  $\text{FePO}_4$  is located at 7114.2 eV,<sup>27</sup> which is 2.3 eV higher than that of  $\text{Fe}^{2+}$  in  $\text{LiFePO}_4$ . This is ascribed to the fact that the electrons in  $\text{Fe}^{3+}$  ions are strongly bound to the nucleus, inducing the shift of  $1s \rightarrow 3d$  transitions to a higher energy level.

X-ray absorption O *K*-edge spectra were measured in both electron-yield and X-ray fluorescence-yield modes (EY and FY, respectively). It is known that the former measurement reflects surface properties of the sample because the escape depth of the electrons is limited to below 50 Å, while X-ray fluorescent detection with a

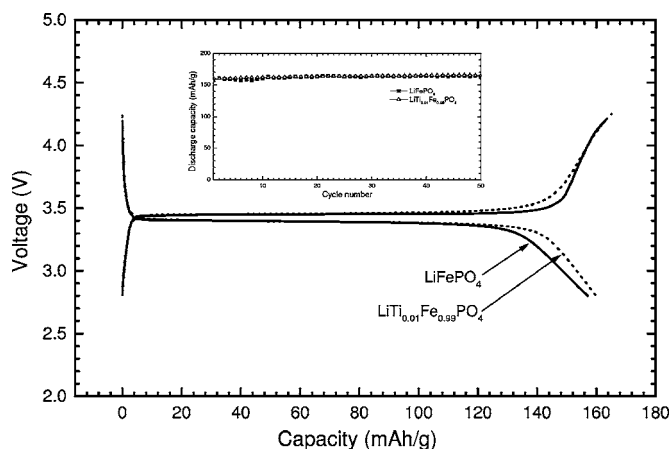


**Figure 7.** The charge/discharge profiles in the first cycle for  $\text{LiFePO}_4$  and doped  $\text{LiTi}_{0.01}\text{Fe}_{0.99}\text{PO}_4$  electrodes. The inset shows the discharge capacity vs cycle number.

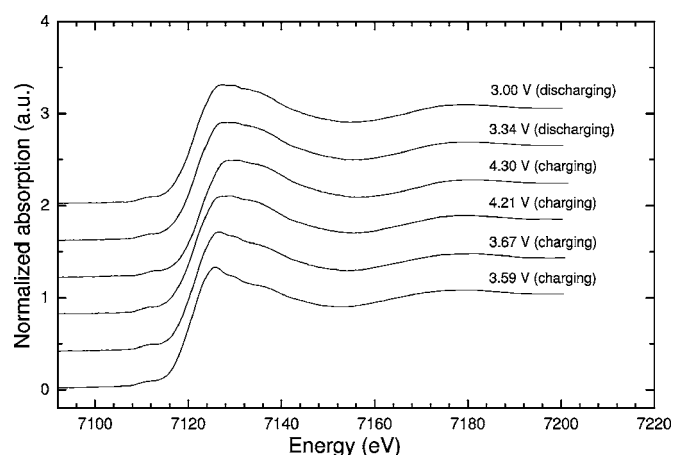


**Figure 8.** In situ Fe *K*-edge XANES spectra of  $\text{LiFePO}_4$  electrode at different charge and discharge states.

probing depth of thousands of angstroms reflects bulk properties of the material. Oxygen *K*-edge X-ray absorption spectra of undoped and Ti-doped samples are shown in Fig. 5a and b.

Based on O 1s X-ray absorption measurements of  $\text{LiFePO}_4$  doped with Ti, Al, and Cu by Abbate et al.,<sup>28</sup> an extra absorption feature just below O 1s absorption threshold was observed which corresponds to the transition to O 2p mixed with Fe 3d states, and reflects formation of doping-induced states in the bandgap of  $\text{LiFePO}_4$ . Our results of O 1s XANES spectra are similar to those reported by Abbate et al. However, if one compares O *K*-edge spectra measured in EY and FY modes, the difference in absorption intensities between undoped and doped samples is more pronounced in the case of EY measurements. Taking into account that EY X-ray absorption measurements reflect the surface layer properties, it is obvious that surface and bulk properties of Ti-doped  $\text{LiFePO}_4$  differ from each other much more than those for the sample without doping. This result agrees well with Fe *K*-edge XANES data, where increase in the white line intensity was explained by an enhanced hole concentration of the surface.

Iron *L*-edge XAS spectra of the two compounds studied, which were measured in electron yield mode, are shown in Fig. 5c. The different ratio between intensities of absorption peaks at 707 and 709 eV also reflects the increase of  $\text{Fe}^{3+}$  concentration increase on the surface of Ti-doped sample.  $\text{LiFePO}_4$  is considered to be a highly stoichiometric compound which is not disposed towards oxygen or lithium ions defect formation due to high stability of  $\text{PO}_4$

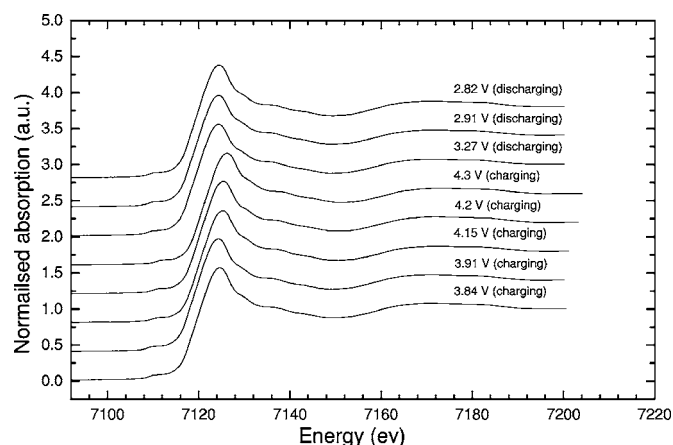


**Figure 9.** In situ Fe *K*-edge XANES spectra of  $\text{LiTi}_{0.01}\text{Fe}_{0.99}\text{PO}_4$  electrode at different charge and discharge states.

**Table III. The pre-edge peak position vs charge/discharge state for LiFePO<sub>4</sub> sample.**

Charge/discharge state	3.59 V (charge)	3.67 V (charge)	4.21 V (charge)	4.3 V (charge)	3.34 V (discharge)	3.0 V (discharge)
Pre-edge peak position (eV)	7112.2	7112.5	7113.1	7113.2	7112.1	7112.0

tetrahedra framework. This is manifested, for example, by two-phase reaction of Li-ion extraction/insertion. Recently, it has been shown by Delacourt et al. that solid solutions exist on the phase diagram at elevated temperatures.<sup>29</sup> It is also known that lithium can evaporate relatively easily at high temperatures during LiFePO<sub>4</sub> preparation. Accordingly, some authors use Li-enriched mixtures of starting reagents for lithium iron phosphate preparation. We cannot exclude the possibility that, during LiFePO<sub>4</sub> synthesis, if some loss of lithium occurs, the surface of the particles will have lower Li concentration compared to the bulk of material. Solid solutions Li<sub>1-x</sub>FePO<sub>4</sub> or ferric orthophosphate FePO<sub>4</sub>, both containing Fe<sup>3+</sup> ions, will thus dominate on the surface. The increased hole concentration on the surface of Ti-doped sample, which is proportional to Fe<sup>3+</sup> content, can be understood if Ti doping leading to Li-ion deficiency formation according to Reaction 2 facilitates Li ions escaping from the surface of the particles. These species also might be responsible for observed XAS spectral features.

**Electrochemical performance of LiFePO<sub>4</sub> and LiTi<sub>0.01</sub>Fe<sub>0.99</sub>PO<sub>4</sub>.**—Cyclic voltammetry measurements were performed on LiFePO<sub>4</sub> and LiTi<sub>0.01</sub>Fe<sub>0.99</sub>PO<sub>4</sub> electrodes to identify the characteristics of the redox reactions in Li-ion cells. Figure 6 shows the cyclic voltammograms of both undoped and doped cathodes. The reduction and oxidation peak positions for LiFePO<sub>4</sub> and doped LiTi<sub>0.01</sub>Fe<sub>0.99</sub>PO<sub>4</sub> cathodes are the same, at 3.34 V and 3.52 V, respectively, vs Li/Li<sup>+</sup>. This elucidates that the Fe<sup>2+</sup>/Fe<sup>3+</sup> redox pairs contribute to the gain and loss of electrons in both LiFePO<sub>4</sub> and doped LiTi<sub>0.01</sub>Fe<sub>0.99</sub>PO<sub>4</sub> crystal structures during the lithium insertion and extraction processes. However, the intensities of the redox peaks for doped LiTi<sub>0.01</sub>Fe<sub>0.99</sub>PO<sub>4</sub> are much higher than that of LiFePO<sub>4</sub>, indicating the higher electrochemical reactivity of Ti-doped electrodes. The capacity and cyclability of LiFePO<sub>4</sub> and LiTi<sub>0.01</sub>Fe<sub>0.99</sub>PO<sub>4</sub> electrodes were determined by galvanostatic charge/discharge testing at a C/8 rate. Figure 7 shows the voltage profiles of LiFePO<sub>4</sub> and LiTi<sub>0.01</sub>Fe<sub>0.99</sub>PO<sub>4</sub> electrodes in the first cycle. Both electrodes exhibited very flat charge and discharge plateaus. The voltages of the charge and discharge plateaus match the oxidation and reduction peaks in the CV curves. LiFePO<sub>4</sub> cathode and doped LiTi<sub>0.01</sub>Fe<sub>0.99</sub>PO<sub>4</sub> cathode show a discharge capacity of 157 and 160 mAh/g, respectively, in the first cycle (approaching the theoretical capacity of 170 mAh/g). The doped lithium iron phosphate delivered a slightly higher capacity, which was attributable to the enhanced electronic conductivity induced by an increased p-type semiconductivity through the dopant effect as shown in the inset in Fig. 7. Both LiFePO<sub>4</sub> and doped LiTi<sub>0.01</sub>Fe<sub>0.99</sub>PO<sub>4</sub> cathodes demonstrate excellent cycle life.

**In situ XANES measurement of LiFePO<sub>4</sub> and LiTi<sub>0.01</sub>Fe<sub>0.99</sub>PO<sub>4</sub> electrodes.**—In order to verify the variation of the Fe oxidation state, we performed in situ Fe K-edge XANES measurements on LiFePO<sub>4</sub> and doped LiTi<sub>0.01</sub>Fe<sub>0.99</sub>PO<sub>4</sub> electrodes during the charge and discharge processes. Figure 8 and Fig. 9 show the in situ Fe K-edge XANES of LiFePO<sub>4</sub> and LiTi<sub>0.01</sub>Fe<sub>0.99</sub>PO<sub>4</sub> electrodes, respectively, at various charging and discharging states, respectively.

Table III and Table IV list the energy positions of the Fe pre-edge peaks for LiFePO<sub>4</sub> and LiTi<sub>0.01</sub>Fe<sub>0.99</sub>PO<sub>4</sub> electrodes, respectively. In general, the Fe K pre-edge peak positions shift to higher energy during the charging process indicating an increased Fe valence, and shift back to lower energy corresponding to a decreased Fe valence on discharging. However, the variation of the Fe K pre-edge peak energy is not entirely linear with respect to the charging and discharging states. Wilk et al.<sup>30</sup> previously studied the Fe K-XANES spectra of various Fe minerals, and concluded that there is considerable nonlinearity in the variation of the pre-edge peak position if both the Fe oxidation state and coordination vary simultaneously. During the charging process, lithium ions were extracted from LiFePO<sub>4</sub>, resulting in the formation of FePO<sub>4</sub>, which has the same framework as LiFePO<sub>4</sub>. However, ex situ neutron powder diffraction and in situ X-ray diffraction have identified a considerable variation of the Fe–O distance between LiFePO<sub>4</sub> and FePO<sub>4</sub>.<sup>31,32</sup> This discrepancy in the Fe–O bond distance could induce a change of local coordination environment for the Fe ions. In the fully charged state, LiFePO<sub>4</sub> and LiTi<sub>0.01</sub>Fe<sub>0.99</sub>PO<sub>4</sub> electrodes are supposed to be electrochemically delithiated to FePO<sub>4</sub> and Ti<sub>0.01</sub>Fe<sub>0.99</sub>PO<sub>4</sub>. We observed a Fe K pre-edge peak at 7113.2 eV for LiFePO<sub>4</sub> and 7113.1 eV for LiTi<sub>0.01</sub>Fe<sub>0.99</sub>PO<sub>4</sub> at the fully charged state, which is slightly lower as compared to the synthetic FePO<sub>4</sub> powder sample.<sup>32</sup> The differences in the Fe K pre-edge peak energy could be due to the structural variation between electrochemically formed FePO<sub>4</sub> and synthetic FePO<sub>4</sub> powders. There was no change of the Fe K pre-edge peak, elucidating no variation of Fe<sup>2+</sup> coordination environment during delithiation and lithiation process. Deb et al. have also performed in situ XAFS measurement on LiFePO<sub>4</sub> electrode. They concluded that during charging of Li<sub>x</sub>FePO<sub>4</sub> to 4 V the oxidation state of Fe changes from (II) to (III) with retention of the Fe–O octahedral symmetry.<sup>33</sup> Previously, there was a report that oxygen, rather than transition metal ions in cathode materials, functions as electron acceptor upon insertion of Li.<sup>34</sup> Here, the in situ XANES measurements show that Fe ions in LiFePO<sub>4</sub> or Ti-doped LiFePO<sub>4</sub> function as electron donor and acceptor during the charging and discharging processes.

## Conclusions

The structural and electrochemical properties of LiFePO<sub>4</sub> and Ti-doped LiTi<sub>0.01</sub>Fe<sub>0.99</sub>PO<sub>4</sub> cathode materials synthesized via a sol-gel process were systematically investigated. The Ti doping results in an increased p-type semiconductivity for LiFePO<sub>4</sub> compounds, which has been confirmed by Fe K-edge XANES, O K-edge and Fe L-edge XAS spectra measurements. The as-prepared lithium iron phosphates demonstrated good electrochemical performance as cathodes in lithium-ion cells. In situ XANES measurements show a variation of Fe valence during the charging and discharging processes without changing of Fe octahedral coordination symmetry.

**Table IV. The pre-edge peak position vs charge/discharge state for LiTi<sub>0.01</sub>Fe<sub>0.99</sub>PO<sub>4</sub> sample.**

Charge/discharge state	3.84 V (charge)	3.91 V (charge)	4.15 V (charge)	4.2 V (charge)	4.3 V (charge)	3.27 V (discharge)	2.91 V (discharge)	2.82 V (discharge)
Pre-edge peak position (eV)	7112.1	7112.6	7112.8	7113.0	7113.1	7112	7111.6	7111.5



### Acknowledgment

The authors acknowledge financial support provided by the Australian Research Council through the ARC Centre for Nano-structured Electromaterials and ARC Linkage project LP0453766.

University of Wollongong assisted in meeting the publication costs of this article.

### References

1. J.-M. Tarascon and M. Armand, *Nature (London)*, **414**, 359 (2001).
2. J. M. Tarascon, E. Wang, F. K. Shokoohi, W. R. McKinnon, and S. Colson, *J. Electrochem. Soc.*, **138**, 2859 (1991).
3. M. M. Thackeray, *J. Electrochem. Soc.*, **142**, 2558 (1995).
4. G. H. Li, H. Ikuta, T. Uchida, and M. Wakihara, *J. Electrochem. Soc.*, **143**, 178 (1996).
5. G. X. Wang, D. H. Bradhurst, S. X. Dou, and H. K. Liu, *Solid State Ionics*, **120**, 95 (1999).
6. J. R. Dahn, U. von Sacken, M. W. Jaskow, and H. Al-Janaby, *J. Electrochem. Soc.*, **139**, 2207 (1991).
7. T. Ozuku, A. Ueda, and M. Nagayama, *Solid State Ionics*, **140**, 1862 (1993).
8. G. X. Wang, S. Zhong, D. H. Bradhurst, S. X. Dou, and H. K. Liu, *Solid State Ionics*, **116**, 271 (1999).
9. A. R. Armstrong and P. G. Bruce, *Nature (London)*, **381**, 499 (1996).
10. B. Ammundsen, J. Desilvestro, T. Groutso, D. Hassell, J. B. Metson, E. Regan, R. Steiner, and P. J. Pickering, *J. Electrochem. Soc.*, **147**, 4078 (2000).
11. Z. P. Guo, S. Zhong, G. X. Wang, G. Walter, H. K. Liu, and S. X. Dou, *J. Electrochem. Soc.*, **149**, A792 (2002).
12. R. Kanno, T. Shirane, Y. Inaba, and Y. Kawamoto, *J. Power Sources*, **68**, 145 (1997).
13. Y. Sakurai, H. Arai, S. Okada, and J. Yamaki, *J. Power Sources*, **68**, 711 (1997).
14. A. K. Padhi, K. S. Nanjundaswamy, and J. B. Goodenough, *J. Electrochem. Soc.*, **144**, 1188 (1997).
15. A. K. Padhi, K. S. Nanjundaswamy, C. Masquelier, S. Okada, and J. B. Goodenough, *J. Electrochem. Soc.*, **144**, 1609 (1997).
16. A. Yamada, S. C. Chung, and K. Hinokuma, *J. Electrochem. Soc.*, **148**, A224 (2001).
17. E. M. Bauer, C. Bellitto, M. Pasquali, P. P. Prosini, and G. Righini, *Electrochem. Solid-State Lett.*, **7**, A85 (2004).
18. G. X. Wang, S. Bewlay, J. Yao, J. H. Ahn, S. X. Dou, and H. K. Liu, *Electrochem. Solid-State Lett.*, **7**, A503 (2004).
19. F. Croce, A. D. Epifanio, J. Hassoun, A. Deptula, J. Olczac, and B. Scrosati, *Electrochem. Solid-State Lett.*, **5**, A47 (2002).
20. P. P. Prosini, D. Zane, and M. Pasquali, *Electrochim. Acta*, **46**, 3517 (2001).
21. S. Y. Chung, J. T. Bloking, and Y. M. Chiang, *Nat. Mater.*, **1**, 123 (2002).
22. P. S. Herle, B. Ellis, N. Coombs, and L. F. Nazar, *Nat. Mater.*, **3**, 147 (2004).
23. A. C. Larson and R. B. von Dreele, *General Structure Analysis System*, Los Alamos National Laboratory, Los Alamos, NM (1994).
24. A. N. Mansour, J. W. Cook, and D. E. Sayers, *J. Phys. Chem.*, **88**, 2330 (1984).
25. H. Yoshitake, T. Mochizuki, O. Yamazaki, and K. Ota, *J. Electroanal. Chem.*, **361**, 229 (1993).
26. A. Deb, U. Bergmann, E. J. Cairns, and S. P. Cramer, *J. Phys. Chem. B*, **108**, 7046 (2004).
27. G. Berlier, G. Spoto, P. Fiescaro, S. Bordiga, A. Zecchina, E. Giamello, and C. Lamberti, *Microchem. J.*, **71**, 101 (2002).
28. M. Abatte, S. M. Lala, L. A. Montoro, and J. M. Rosolen, *Electrochem. Solid-State Lett.*, **8**, A288 (2005).
29. C. Delacourt, P. Poizot, J.-M. Tarascon, and C. Masquelier, *Nat. Mater.*, **4**, 254 (2005).
30. M. Wilke, F. Farges, P. E. Pett, G. E. Brown, Jr., and F. Martin, *Am. Mineral.*, **86**, 714 (2001).
31. A. S. Andersson, B. Kalska, L. Håggström, and J. O. Thomas, *Solid State Ionics*, **130**, 41 (2000).
32. A. S. Andersson and J. O. Thomas, *J. Power Sources*, **97-98**, 498 (2001).
33. A. Deb, U. Bergmann, E. J. Cairns, and S. P. Cramer, *J. Synchrotron Radiat.*, **11**, 497 (2004).
34. G. Ceder, Y.-M. Chiang, D. R. Sadoway, M. K. Aydinol, Y.-I. Jang, and B. Huang, *Nature (London)*, **392**, 694 (1998).